Plasmonics (2019) 14:1269–1281
https://doi.org/10.1007/s11468-019-00916-x

A Route to Unusually Broadband Plasmonic Absorption Spanning from Visible to Mid-infrared

Majid Aalizadeh[1,2] · Amin Khavasi[3] · Andriy E. Serebryannikov[4,5] · Guy A. E. Vandenbosch[4] · Ekmel Ozbay[1,2,6,7]

Received: 20 October 2018 / Accepted: 14 January 2019 / Published online: 5 February 2019

Abstract

In this paper, a route to ultra-broadband absorption is suggested and demonstrated by a feasible design. The high absorption regime (absorption above 90%) for the suggested structure ranges from visible to mid-infrared (MIR), i.e., for the wavelength varying from 478 to 3278 nm that yields an ultra-wide band with the width of 2800 nm. The structure consists of a top-layer-patterned metal-insulator-metal (MIM) configuration, into the insulator layer of which, an ultra-thin 5 nm layer of manganese (Mn) is embedded. The MIM configuration represents a Ti-Al_2O_3-Ti tri-layer. It is shown that, without the ultra-thin layer of Mn, the absorption bandwidth is reduced to 274 nm. Therefore, adding only a 5 nm layer of Mn leads to a more than tenfold increase in the width of the absorption band. It is explained in detail that the physical mechanism yielding this ultra-broadband result is a combination of plasmonic and non-plasmonic resonance modes, along with the appropriate optical properties of Mn. This structure has the relative bandwidth (RBW) of 149%, while only one step of lithography is required for its fabrication, so it is relatively simple. This makes it rather promising for practical applications.

Keywords Localized surface plasmons · Nanodisk array · Impedance matching · Guided-mode resonance

Introduction

Electromagnetic (EM) absorbers have gained a lot of attention due to their wide applications in various fields, including photovoltaics [1, 2], sensing [3, 4], photodetection [5, 6], thermal imaging [7], thermal emission [8], and shielding [9, 10]. The concept of metamaterials has made it possible to come up with EM absorbers with a subwavelength thickness. Such subwavelength EM absorbers are reported in various frequency regimes that include microwave [11], terahertz [12, 13], far-infrared (FIR) [14], mid-infrared (MIR) [15], near-infrared (NIR) [16], and visible [17, 18].

Absorption can be realized by trapping the light in an EM resonance mode and dissipating its power through the intrinsic loss of materials. The typical resonance modes used in absorbers include localized surface plasmon (LSP) [19, 20], propagating surface plasmon (PSP) [21, 22], and Fabry-Perot resonance [23, 24] modes. Broadband metamaterial absorbers have all the earlier mentioned applications, except for sensing. This is obviously because of the fact that in order to achieve a better sensing functionality, a narrower resonance is typically desired [25]. The main approaches for obtaining broadband absorption are either through broadening the resonance mode or by using the superposition of several adjacent resonances, or a combination of both. Broadening the resonances is equivalent to decreasing the quality factor of the resonance mode. This is possible by the appropriate adjustment of geometrical parameters and through the use of metals with high loss.

It is also possible to obtain perfect absorption while not having any specific resonance mode. It can be realized by blocking both the transmission and reflection. The transmission can be

✉ Majid Aalizadeh
majid.aalizadeh@bilkent.edu.tr

1 Department of Electrical and Electronics Engineering, Bilkent University, 06800 Ankara, Turkey

2 Nanotechnology Research Center (NANOTAM), Bilkent University, 06800 Ankara, Turkey

3 Electrical Engineering Department, Sharif University of Technology, Tehran 11155-4363, Iran

4 ESAT-TELEMIC, Katholieke Universiteit Leuven, 3000 Leuven, Belgium

5 Faculty of Physics, Adam Mickiewicz University, 61-614 Poznan, Poland

6 National Nanotechnology Research Center (UNAM), Bilkent University, 06800 Ankara, Turkey

7 Department of Physics, Bilkent University, 06800 Ankara, Turkey

blocked by using an optically thick metal layer as the most bottom layer of the structure, and the reflection can be suppressed by providing impedance matching with free space [13, 26]. Therefore, it is possible to have perfect absorption by impedance matching and without any resonance mode. This is mostly useful for absorbing at the wavelengths that are much larger than the dimensions of the array's unit-cell.

In one of the early works on broadband absorbers, Aydin et al. experimentally achieved 71% average absorption in the visible (400–700 nm) range [27]. It was obtained using nanorods with a non-uniform (tapered) width, which led to the superposition of various LSP resonances, each corresponding to a specific width. There are also some lithography-free (non-arrayed) broadband absorbers that are fabricated by our group by the use of dewetting mechanism [28]. Dewetting is a method, in which ultra-thin layers are annealed at high temperatures to deform into nanoholes or nanoparticles, depending on the annealing recipe [29]. The nanoholes or nanoparticles with random sizes then lead to having the superposition of LSP modes, each corresponding to a specific nanoparticle size. There is also another recent lithography-free work carried out in our group, in which a broadband absorption was achieved by the superposition of LSP resonances of the randomly oriented dielectric-metal core-shell nanowires [30]. Broadening the Fabry-Perot resonance mode has also been extensively studied in MIM cavities [31, 32] and metal-insulator stacks [33].

One of the commonly used absorber structures is the MIM structure, in which the top metal layer is patterned using lithography. In one of the recent works, Au-SiO_2-Ti configuration is used in the MIM structure, and the top Ti layer is patterned as a periodic array of nanodisks [16]. The high absorption band in that structure is extended over the wavelength range of 900 to 1825 nm with a 71% relative bandwidth that is defined as the ratio of the high absorption bandwidth to the center wavelength.

In this work, we show that, by embedding an ultra-thin 5 nm layer of Mn into the dielectric layer of a typical top-layer-patterned MIM structure (with a 2D array of nanodisks on the top), an ultra-broadband, nearly perfect absorption (greater than 0.9) can be obtained over the wavelength range of 478 to 3278 nm. The bandwidth and relative bandwidth of the proposed structure are 2800 nm and 149%, respectively, and the absorption band extends over the visible, NIR, and MIR regions. This is, to our knowledge, the best result obtained for such absorbers with one-stage lithography. The absorption band of the MIM structure without the ultra-thin Mn layer covers the two adjacent ranges of 478 to 526 nm and 610 to 836 nm that is equivalent to 274 nm of total bandwidth. Therefore, adding a thin layer of Mn, leads to a 10.1-fold increase in the bandwidth, without adding much complexity or lithography stage to the fabrication process. A step-by-step dimension and material optimization procedure is presented. We investigate different types of metals in order to find the most appropriate ones for an ultra-wideband absorber. We also consider the effect of the dimensions of the structure on the absorption bandwidth. Then, the physical mechanisms that lead to strong absorption in different wavelength ranges are discussed. In particular, we discuss in detail the importance of the 5 nm Mn layer for the significant increase of the bandwidth of the structure. This is while Mn has not been given the attention it deserves for the use in broadband absorbers. Mn was used for the first and, up to now, the only time in a broadband absorber structure that was recently fabricated in our group, and it led to a very promising result compared to other metals [32]. Moreover, we demonstrate the high fabrication tolerance of the proposed structure. Finally, we explore the effect of polarization and incidence angle. Numerical results are obtained using the finite difference time domain (FDTD) method by Lumerical FDTD software [34], and the results are verified by regenerating them using the finite integration technique (FIT) by CST Microwave Studio [35].

It is worth mentioning that, because of requiring just one-step lithography, the large-area fabrication of the proposed structure can be realized by the use of the standard nanoimprint lithography technique [36]. This is very beneficial for mass and high-throughput production purposes.

Design and Optimization Procedure

Proposed Structure

The schematic of the proposed absorber is shown in Fig. 1. It consists of an MIM structure with the top and bottom metal layers being chosen as Ti, and Al_2O_3 being used as the dielectric layer, and with the top Ti layer being patterned to obtain a periodic array of nanodisks, while an ultra-thin, 5 nm layer of Mn is embedded into the dielectric layer. As shown in Fig. 1a-c, the period, height of nanodisks, radius of nanodisks, thickness of the Mn layer, the distance between the bottom metal and the top nanodisks, and the distance between the bottom metal and the Mn layer, are denoted by p, h, r, t_{Mn}, d_i, and d_{Mn}, respectively. The bottom metal layer is expected to be sufficiently thick to block transmission. The perspective description of the proposed absorber is shown in Fig. 1d. In this view, the 5 nm Mn layer might be considered as a perturbation that is introduced to the patterned MIM configuration of Ti-Al_2O_3-Ti. This is while, as it will be elevated in the forthcoming sections, the effect of this ultra-thin Mn layer is drastically significant in the enhancement and broadening of the nearly perfect absorption band. The optimized dimensions for the structure, according to Fig. 1, will be chosen in the next sections. They are equal to 480, 140, 180, 165, 5, and 135 nm for p, r, h, d_i, t_{Mn}, and d_{Mn}, respectively. The thickness of the bottom metal layer is conservatively chosen to be 200 nm to

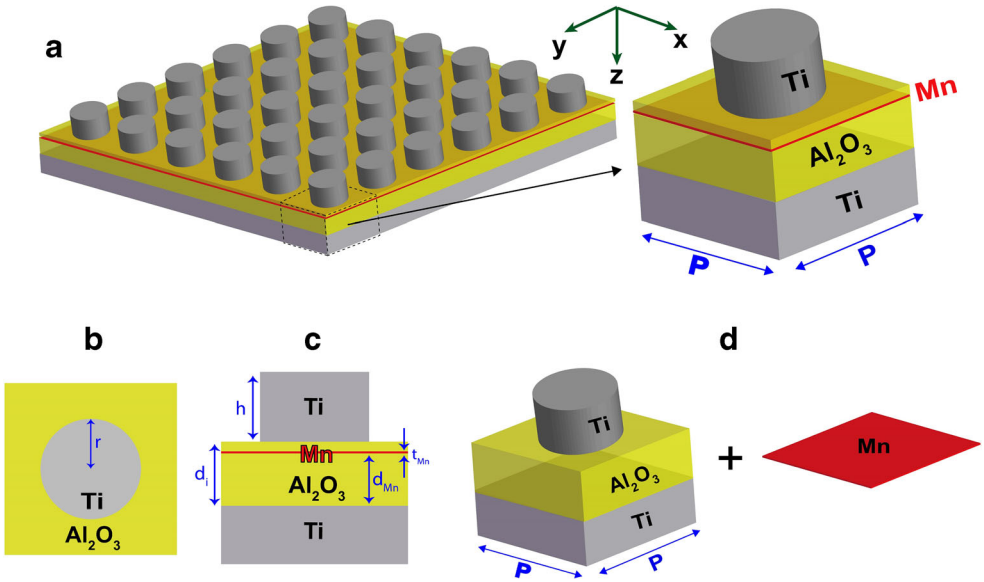

Fig. 1 **a** Left plot: 3D schematic of the absorber; one unit cell of the structure is bounded by dashed lines; right plot: a magnified view of one unit cell. **b** Top view, and **c** side view of the structure; and **d** the other image of the unit cell of the studied structure (perspective view): a patterned MIM configuration with top periodic layer composed of metal nanodisks, plus an ultra-thin Mn layer embedded into the insulator of the original configuration

ensure nearly zero transmission. It should be mentioned that this choice of metals is the result of simulating all the possible combinations of several metals (which are conventionally used in broadband absorbers) in the proposed structure, and performing a thorough study on the results. These metals include chromium (Cr), tungsten (W), platinum (Pt), and iron (Fe), in addition to Ti and Mn.

Material Optimizations

In order to demonstrate the effect of the choice of materials on the performance of the device and optimize the structure in terms of materials, the absorption spectra have been simulated. The results are shown in Fig. 2a–d for the case of only changing the material of the dielectric layer, bottom metal layer, top nanodisks, and the 5 nm ultra-thin middle layer, respectively. All of the other materials and dimensions of the structure were kept unchanged. The thin horizontal dashed line in Fig. 2 corresponds to 90% absorption. The refractive index data of all the metals except Mn, along with Al_2O_3 and SiO_2 are taken from [37], and the refractive index data of Mn, HfO_2, and TiO_2 are taken from [38–40], respectively. Our purpose here is to choose the configuration that gives the widest band, while the bandwidth (BW) is defined as $BW = \lambda_{max}-\lambda_{min}$, where λ_{max} and λ_{min} are the upper and lower wavelength limits of the region, in which absorption is above 90%. The absorption (A) in general case can be obtained given the values of reflectance (R) and transmittance (T), using the formula $A = 1-R-T$, where $R = r^2$ and $T = t^2$ with r and t being reflection and transmission coefficients, respectively. However, since the bottom metallic layer is sufficiently thick to suppress transmission (200 nm), the absorption formula simplifies to $A = 1-R$.

Let us first consider the effect of dielectric material on the absorption spectrum. The dielectrics chosen to be used in this investigation are SiO_2, Al_2O_3, HfO_2, and TiO_2, which are listed here from the smallest to the largest refractive index, respectively. It can be observed in Fig. 2a that by choosing dielectrics with higher refractive index, almost all the absorption peaks experience a redshift. This is already expected to happen because of the nature of the resonance modes [41]. This figure demonstrates that the best bandwidth is obtained for the case of using Al_2O_3 as the dielectric material. For the case of changing the materials of the bottom metal and the top nanodisks, as shown in Fig. 2b, c, respectively, it can be noticed that the absorption does not experience drastic changes. This shows that the absorption capability of the entire structure, when taking the bottom layer and top nanodisks into account, dominantly results from the geometric design rather than the choice of materials. However, about the middle metal layer, which is taken as 5 nm, it can be observed in Fig. 2d that the choice of metal drastically affects the absorption spectrum's shape and bandwidth at wavelengths larger than 800 nm. Therefore, this ultra-thin layer plays an important role in broadening the absorption spectrum in the NIR and MIR regions. The results shown in Fig. 2a-d justify that the choice of the materials in Fig. 1 provides the widest absorption band.

Geometry Optimizations

To demonstrate the effect of the radius of the nanodisks (r) and the period (p), the absorption spectrum is calculated and shown for different values of r, for $p = 440$, 460, 480, 500, 520, and 540 nm, in Fig. 3a–f, respectively. It is noteworthy that the hight of nanodisks (h) is fixed at 180 nm, and the materials are chosen in accordance with Fig. 1. Similarly,

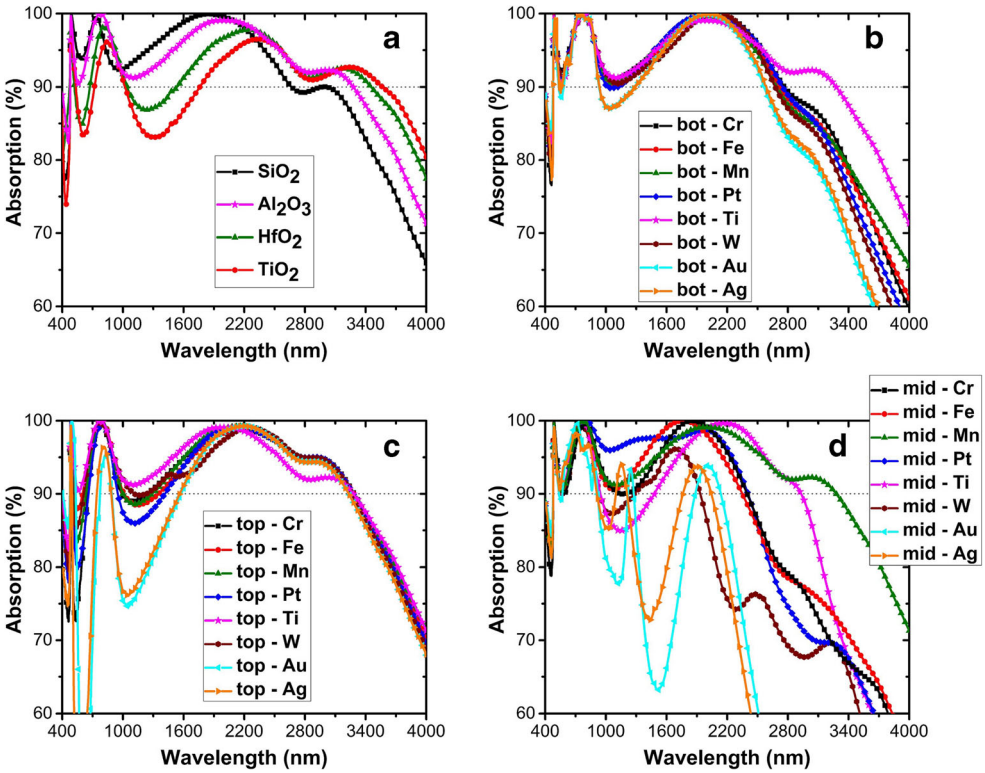

Fig. 2 Absorption spectra for different materials of **a** dielectric layer, **b** bottom metal layer, **c** top metallic nanodisks, and **d** middle ultra-thin metal layer, while using the same materials for the remaining components as in Fig. 1. The dimensions of the structure in all cases are: $p = 480$ nm, $r = 140$ nm, $h = 180$ nm, $d_i = 165$ nm, $t_{Mn} = 5$ nm, and $d_{Mn} = 135$ nm. The geometrical sizes in case of another material of the middle layer than Mn in (d) are the same as in case of Mn

calculations are performed for the case of varying h, and for abovementioned values of p at $r = 140$ nm. The results are shown in Fig. 4a-f.

As shown in Fig. 3, by increasing the radius of nanodisks, the second, third, and fourth absorption maximums are shifted toward larger wavelengths. However, it comes at the cost of

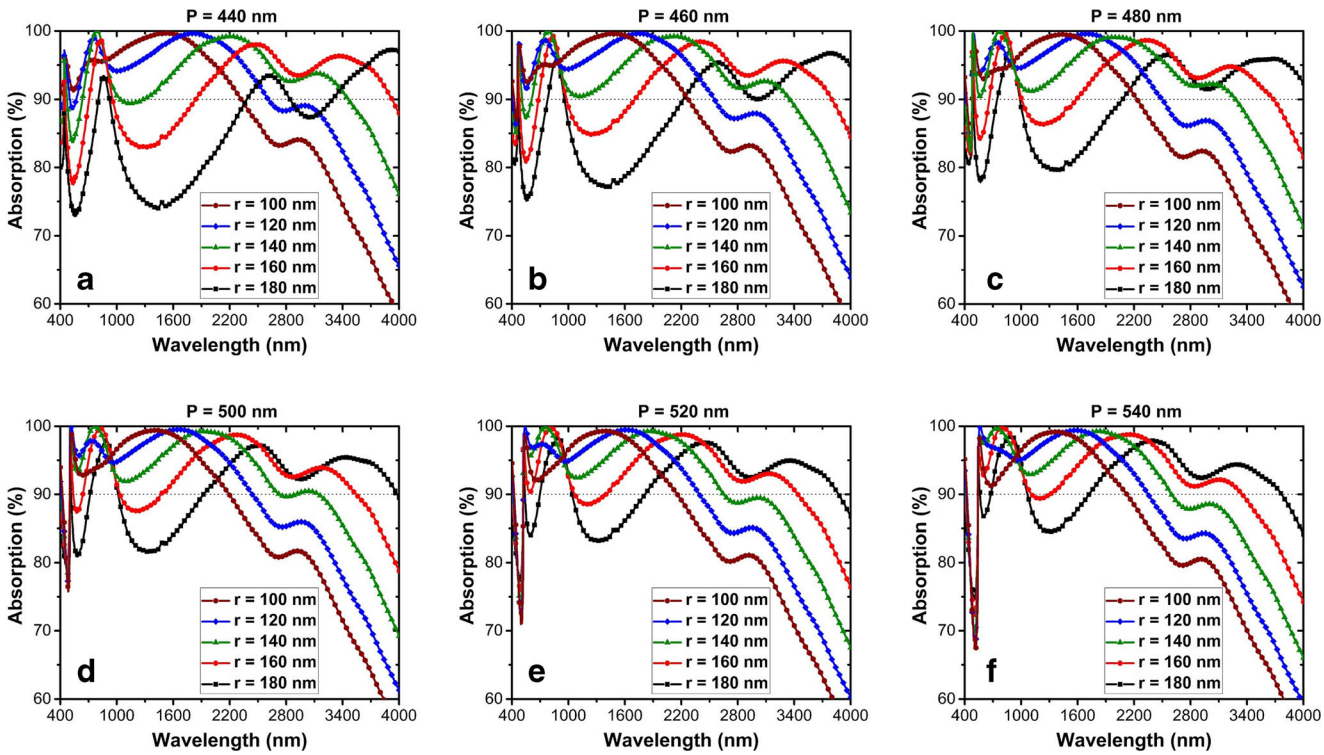

Fig. 3 Absorption spectra of the structure at different values of the radius of nanodisks (r), while period (p) is taken as **a** 440, **b** 460, **c** 480, **d** 500, **e** 520, and **f** 540 nm. In all plots, $h = 180$ nm and the materials are chosen in accordance with Fig. 1

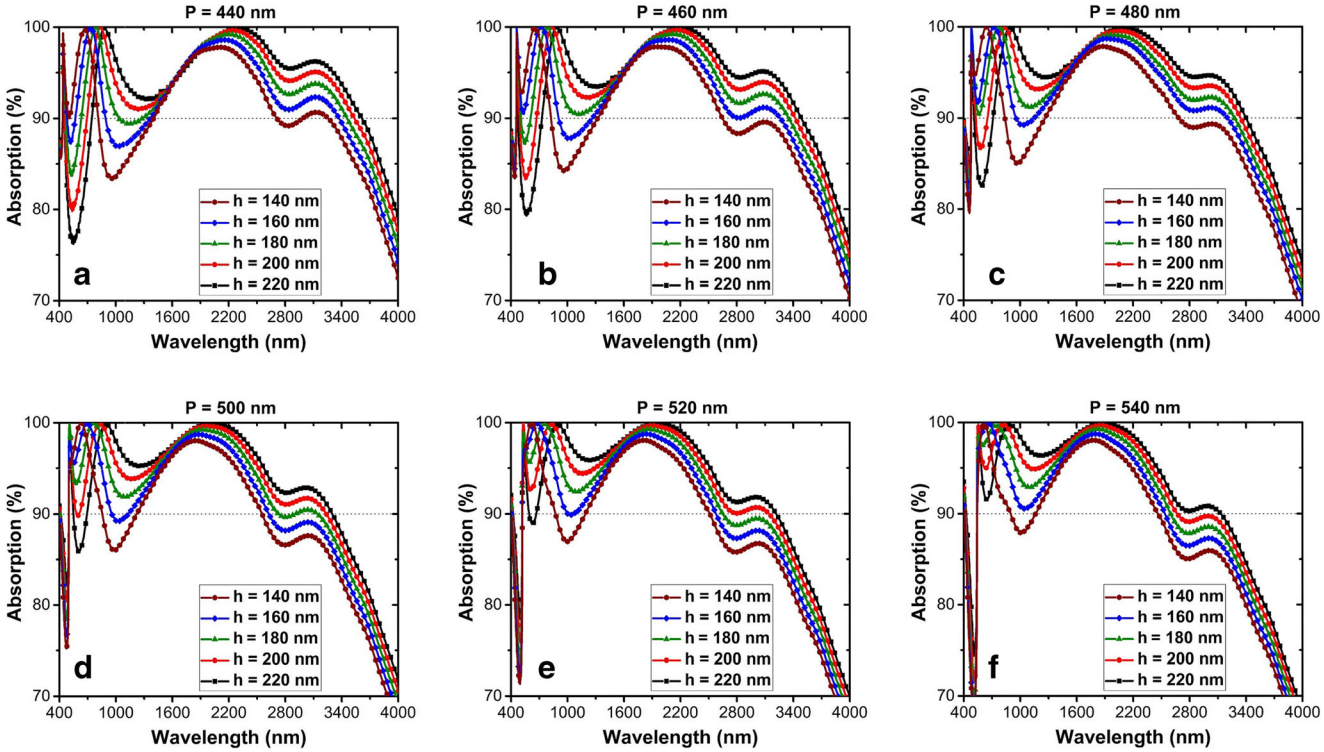

Fig. 4 Absorption spectra of the structure at different values of the height of nanodisks (h), while period (p) is taken as **a** 440, **b** 460, **c** 480, **d** 500, **e** 520, and **f** 540 nm. In all plots, $r = 140$ nm and the materials are chosen in accordance with Fig. 1

losing the strength of absorption at smaller wavelength range. In addition, a comparison of Fig. 3a–f reveals that increasing the period of the structure blueshifts the absorption band and increases the strength of the absorption in small wavelength regime. By comparing the bandwidths for all the presented cases, we choose the case presented in Fig. 3c, where $p =$ 480 nm and $r = 140$ nm, because it provides the largest absorption bandwidth. As can be seen in Fig. 4, the increase in the height of nanodisks exerts qualitatively the same effect on the absorption spectrum as the increase of r. Again, the results show that the best values for h and p are 180 and 480 nm, respectively. Therefore, Figs. 3 and 4 confirm that the optimal values for r, h, and p are 140, 180, and 480 nm, respectively.

Results and Discussions

Absorption of Optimal Design

The absorption spectrum of the optimal structure is plotted in Fig. 5. To verify the FDTD simulations, the absorption of the structure has also been calculated using CST Microwave Studio software, which is based on the FIT. The FDTD and FIT results are shown with solid red and dashed black lines, respectively. It is shown in Fig. 5a that the region of high absorption (above 90%) starts at the visible, covers the whole NIR, and ends at the MIR regime, i.e., it is in the wavelength range extending from 478 to 3278 nm. The bandwidth is then 2800 nm. The relative bandwidth of absorption is calculated by $\mathrm{RBW} = \mathrm{BW}/\lambda_{\mathrm{cent}}$, where BW and λ_{cent} denote the bandwidth and the center wavelength of the absorption band, respectively. For this structure, we obtain RBW = 149%. This is, to our knowledge, the best result obtained for the absorbers with one-stage lithography that may cover a very wide wavelength range, which starts at the visible and ends within the MIR range.

The contribution of each metallic layer (as an absorptive component) to the resulting absorption of the structure versus the wavelength is also plotted in Fig. 5a, where the absorption spectra of the bottom Ti layer, ultra-thin Mn layer, and top Ti nanodisk array are shown by pink, blue, and green lines, respectively. The absorption of each individual layer of the entire structure is calculated by placing the field recording and index recording monitors inside the structure in the simulation, and calculating absorption at multiple observation points inside each layer.

Physical Analysis

In this section, we investigate the physical mechanism behind the observed wideband absorption. As shown in Fig. 5b, the absorption peaks appear at 486, 778, 2027, and 3064 nm. The peak at the wavelength of 3064 nm shows weaker absorption compared to the other peaks, but as it can be seen in Fig. 2d,

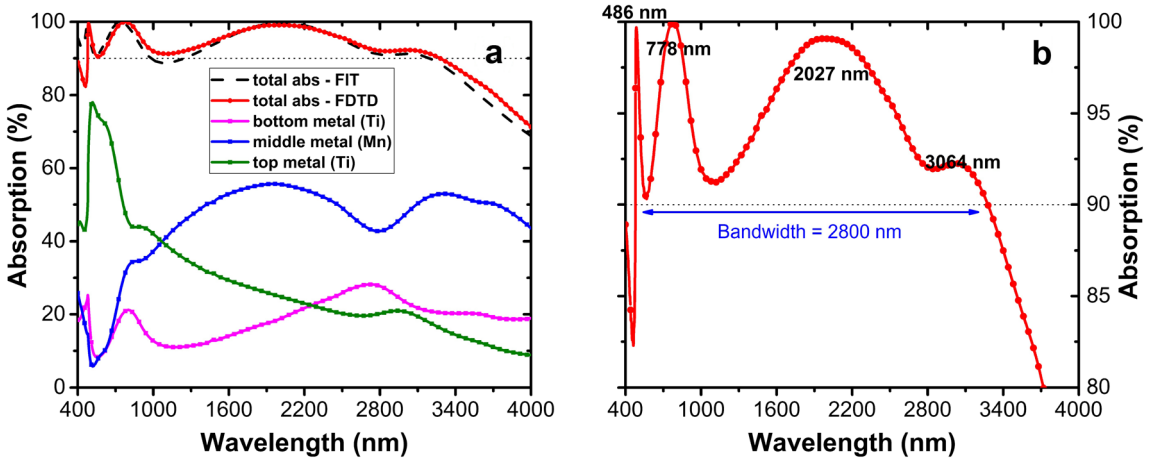

Fig. 5 **a** Absorption spectra of the optimal structure calculated by FDTD (solid red line) and FIT (dashed black line) methods, along with contribution of each metallic layer to the absorption of the entire structure, and **b** absorption of the optimal structure (FDTD results) with magnified ordinate axis, to clearly demonstrate the peak positions and bandwidth of the absorption

this peak helps the nearly perfect absorption bandwidth to increase significantly compared to the other possible choices of metals for the ultra-thin layer. Therefore, it is worth discussing the physical mechanism behind this peak, and compare with the other peaks.

As the first step, we consider the absorption of each metallic layer versus the wavelength as shown in Fig. 5a. It can be observed that at smaller wavelengths, up to around 1000 nm, the absorption in the Ti nanodisks dominates the absorption of the Mn layer and the bottom Ti layer. This conveys that the absorption at smaller wavelengths must be mainly due to some resonance modes occurring owing to the nanodisks. These resonances may lead to the absorption of light around the nanodisks, which are made of Ti, a highly lossy metal. On the other hand, at larger wavelengths, i.e., nearly after 1000 nm, a great portion of light is absorbed by the ultra-thin, 5 nm layer of Mn, while the absorption portions of the Ti nanodisks and the thick bottom Ti layer are relatively smaller. This occurs despite the fact that the both Ti components have a much larger thickness than the Mn layer. This again signifies the crucial role of the Mn layer in the broadness of the absorption spectrum that is achieved in the studied structure.

To better illustrate importance of the 5 nm Mn layer, we investigate the optical response of the suggested structure without this layer, i.e., when Mn is replaced by Al_2O_3 and the remaining structure is a top-layer-patterned MIM configuration. The schematic of the structure without the ultra-thin Mn layer is presented in Fig. 6a (also see Fig. 1d). The absorption spectra of the structures with and without the Mn layer are shown, respectively, by red and blue lines in Fig. 6b. The absorption band extends from 478 to 526 nm and from 610 to 836 nm for the configuration without the Mn layer, i.e., it is composed of two adjacent bands. Although the absorption spectrum has four peaks at the wavelengths of 482, 722, 2320, and 2848 nm in this case, the third peak does not have a significant strength. Therefore, the resulting absorption band is relatively narrow (it comprises the abovementioned adjacent bands) with the total bandwidth of 274 nm, in the case of not using the Mn layer. After adding the Mn layer, the strength and the spectral position of the first two peaks do not change significantly, but the strength of the third and fourth peaks considerably increase, and they also experience some shift that is depicted in Fig. 6b with the black arrows. This conveys that the first and second absorption peaks do not depend on the effect exerted by the Mn layer, while the third and fourth ones are significantly affected by the Mn layer. This is in total agreement with our observations in Figs. 5a and 2d. Then, by adding the Mn layer, the bandwidth gets enhanced from 274 to 2800 nm, i.e., it experiences a tenfold increase. It is worth noting that adding an ultra-thin layer of Mn to the structure does not add considerable complexity to the fabrication process.

The absorption peaks may occur due to different types of resonances such as LSP, PSP, or guided-mode resonance (GMR). The LSP resonances may occur due to the properties of individual nanodisks and their coupling [16], the PSP mode can propagate at the continuous interface of the bottom Ti layer and Al_2O_3 layer [17], and GMR can appear in the Al_2O_3 layer that can work as a dielectric waveguide starting from a certain value of d_i [42–44]. It is noteworthy that as follows from the results of simulations performed for different materials of the dielectric layer (i.e., other than Al_2O_3) and its thickness, GMRs may provide the main contribution to the resulting mechanism behind the first peak, in some ranges of variation of the geometrical and material parameters, while PSPs do so for other ranges. Moreover, it has been observed that the GMR-related and the PSP-related effects may coexist in one structure at the same frequency, and sometimes it is difficult to distinguish between the extents, to which each of them contributes. For instance, based on our simulations, the

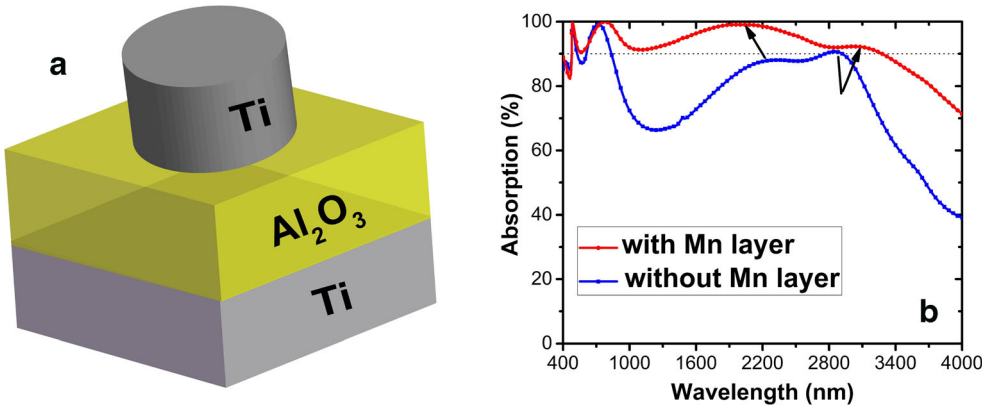

Fig. 6 **a** 3D schematic of the unit cell of the structure without the Mn layer, and **b** absorption of the optimal structure with and without the Mn layer shown by red and blue lines, respectively

dominant effect of a PSP for the first peak is obvious in case of a thinner Al_2O_3 layer (e.g., at $d_i = 80$ nm). In such a case, the field pattern is similar to the one in [17]. At the same time, as will be exemplified below for our optimal parameters, a GMR can dominate at larger thicknesses of the dielectric layer. As the full classification of the possible physical effects and an estimation of the extent of their possible contribution to the resulting absorption mechanism are beyond the scope of this paper, we focus here on the optimal (main) structure.

In order to obtain some vision of the physical phenomena underlying the observed absorption peaks, the distribution of magnetic field inside the structure at the xz-plane cross section of the unit cell (see Fig. 1c) is presented in Fig. 7. Fig. 7a–d show the H-field pattern at the first, second, third, and fourth absorption peak's wavelength, respectively. Because of the symmetry properties of the designed structure, it is polarization insensitive for the case of normal incidence. Without any loss of generality, we may assume the electric field vector of the normally incident wave to be in the x-direction, see Fig. 1a. Therefore, since the propagation is in the z-direction, its magnetic field vector is in the y-direction. Field distributions in Fig. 7 show the y-component of the magnetic field (H_y) at the four peak wavelengths of the main structure. It is noteworthy that for the shown cross section (for which size of a nanodisk is $2r$ in x-direction), the only component of magnetic field is H_y, while H_x and H_z are zero.

It can be observed in Fig. 7a that at the first peak of the main structure, the field is strong in the Al_2O_3 layer that indicates possible connection to a GMR. Moreover, some features are seen, which indicate possible contribution of PSPs at the bottom Al_2O_3-Ti interface. At the second peak, the magnetic field distribution, which is shown in Fig. 7b, indicates some localization around and between the nanodisks, so that the excitation of an LSP mode occurs here due to the properties of Ti disks and coupling between the adjacent disks. Field patterns of the third and fourth peaks shown in Fig. 7c, d are very similar to each other, and both are showing localization of the field under the nanodisks, inside the dielectric layer. For the fourth peak, the field pattern indicates the possible excitation of an LSP mode (or gap plasmon mode) inside the dielectric gap between the underside of nanodisks and bottom Ti layer [17]. Moreover, a strong field enhancement can be observed around the ultra-thin Mn layer and inside it, which may appear due to the optical properties of Mn (will be explained in detail later), that allows the field to penetrate and transmit through the layer easily, and get absorbed inside it. This is why the absorption of the Mn layer is higher compared with the other two metallic components at large wavelengths (see Fig. 5a), and adding the Mn layer enhances the absorption of the entire structure rather at large wavelengths than at the small ones (see Fig. 6b). The situation is similar but not identical for the third peak. In this case, an LSP cannot exist

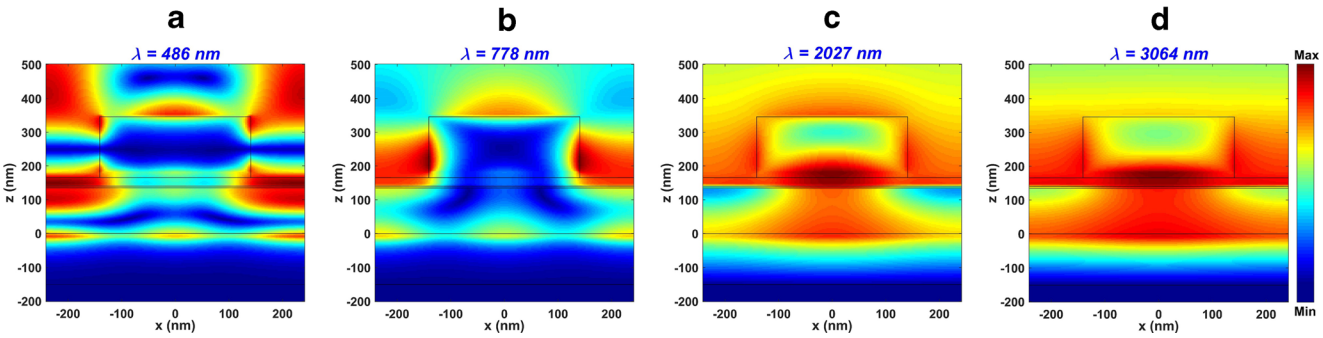

Fig. 7 The spatial distribution of the magnitude of the y-component of the magnetic field (H_y) in the xz cross section of the structure at the **a** first, **b** second, **c** third, and **d** fourth absorption peak

because the real part of permittivity is positive for all of the used materials. In fact, we have an all-dielectric lossy structure in this case. Therefore, we rather have the mimicking of an LSP mode. It might be in qualitative coincidence with the recently suggested theory of surface plasmon-like effects in all-dielectric structures [45], but it needs an additional clarifying.

To demonstrate possible effects of a GMR and an LSP mode, the absorption spectrum of a periodic array of Ti nanodisks on a 165 nm thick Al_2O_3 substrate is plotted in Fig. 8a. The unit cell of the simulated structure is also shown in the inset of the figure and the dimensions are chosen as p = 480, h = 180, r = 140, and d_i = 165 nm. Absorption peaks are observed at 535 and 775 nm, being a reminiscence of the first and second peaks of absorption in the main structure. The spectral location of the peak at 775 nm is very close to the second absorption peak of the main structure at 778 nm. It is because they both appear due to the excitation of a coupled LSP mode between the nanodisks, and in both cases, nanodisks are the same. In turn, the first resonance at 535 nm is associated with a GMR. The reason that its spectral position does not perfectly coincide with the first peak of the main structure is that in the case of GMR, a layer located below the Al_2O_3 layer affects the GMR wavelength. As shown by the obtained results, adding a back-side slab below the Al_2O_3 layer and changing the real part of its permittivity from unity to that of Ti leads to the gradual shift of the first peak closer and closer to the first peak in the main structure (as well as to the one in the main structure but without the Mn layer). This gives us more evidence that the first peak of absorption in the main structure is connected to a GMR.

Next, Fig. 8b shows the absorption spectrum of the structure when the bottom Ti layer is replaced with a perfect electric conductor (PEC). The unit cell of the simulated structure is also shown in the inset of this figure, and the dimensions are the same as those of the optimized structure. This simulation is done to confirm the fact that the first absorption peak of the main structure is due to a GMR, and not a PSP mode. There are two absorption peaks at 477 and 783 nm, which almost perfectly match with the first and second absorption peaks of the main structure at 478 and 778 nm, respectively. This indicates that, in contrast with some of the earlier suggested absorbers [16, 17], these peaks are mainly not due to the excitation of a PSP mode at the bottom Al_2O_3-Ti interface. Indeed, when there is a PEC bottom layer, any PSP mode cannot exist at its interface.

As we mentioned above, the field pattern of the first peak signifies the existence of a GMR. The phase-matching condition of the GMR in the 2D periodic structures is as follows [42, 43]:

$$k_{GMR} = k_0 \sin(\theta_0) + m\left(\frac{2\pi}{p}\right) \quad (1)$$

where p is the period of the structure, θ_0 is the incidence angle, k_{GMR} is the wavenumber of the GMR, k_0 is the wavenumber of the incident wave in the free space, and m is an integer number. It is noteworthy that the similar condition is valid for PSPs in 2D periodic structures [16]. However, we confirmed above that the first peak of absorption for the main structure cannot be due to PSP. Eq. (1) conveys that by increasing (decreasing) the period of the structure, the spectral position of the GMR should experience a redshift (blueshift). To investigate this effect, the absorption spectra of the optimal structure with different values of p have been shown in Fig. 9a. The range of wavelength is taken between 400 and 1000 nm, for better evidence of the shifting behavior for the first two peaks. As expected, the first peak experiences a redshift while increasing p. This confirms our earlier argument that the first peak is connected with a GMR. The second peak experiences almost no shift that indicates no connection to a GMR or PSP.

Let us be reminded that the second peak is due to the excitation of a coupled LSP mode (Fig. 7b), and fourth and third peaks are expected to appear due to the excitation of a gap plasmon LSP mode and the mimicking of such a mode in all-dielectric case, respectively (Fig. 7c and d). Figure 9b, c demonstrate the absorption spectra of the optimal structure for

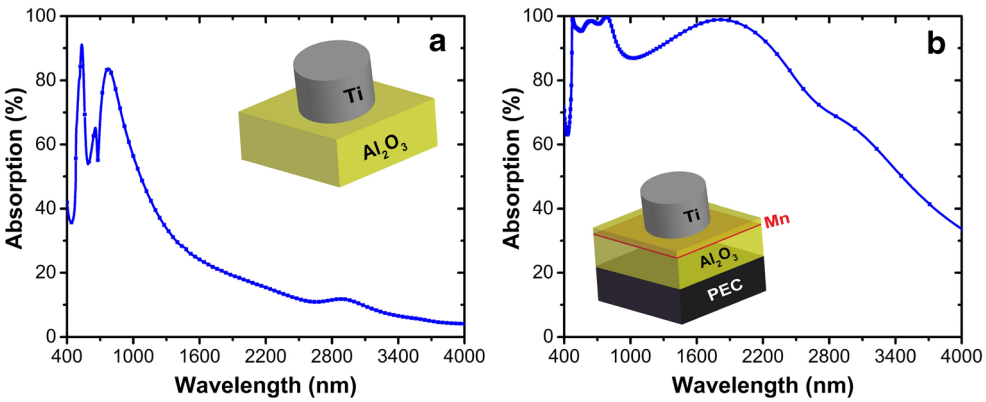

Fig. 8 **a** Absorption spectrum of the periodic array of Ti nanodisks on the Al_2O_3 substrate, with p = 480, h = 180, r = 140, d_i = 165 nm. **b** Absorption spectrum in case when bottom Ti layer is replaced by PEC, with the same dimensions as those of optimized structure. The insets show the schematics of the simulated structures

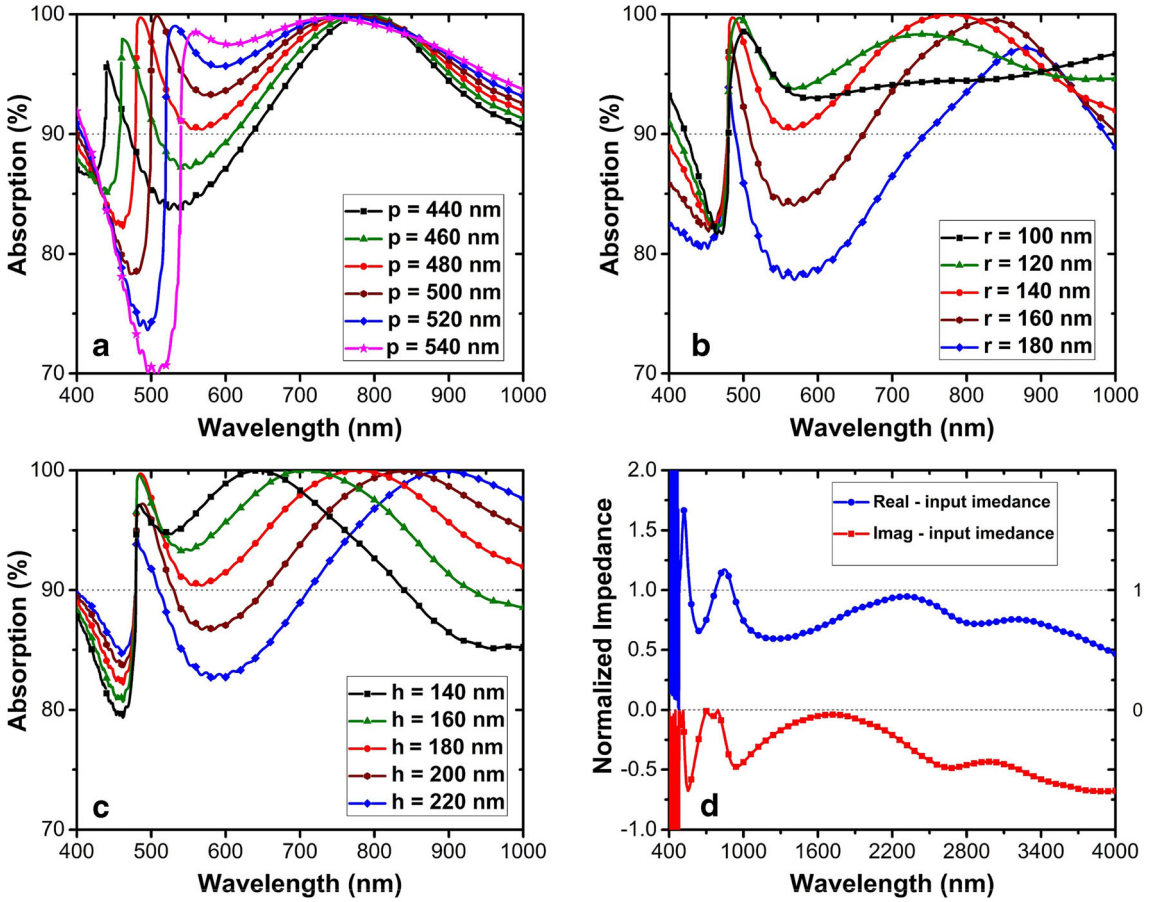

Fig. 9 Absorption spectra of the optimal structure for different values of **a** p, **b** r, and **c** h; **d** real (blue line) and imaginary (red line) parts of the normalized input impedance of the optimal structure, Z_{in}, calculated using S-parameters, see Eq. (2)

different values of r and h, respectively, with the wavelength ranging from 400 to 1000 nm. It can be observed that the increase of r or h causes an obvious redshift in the position of the second peak, while the position of the first peak is almost insensitive to any variation of r and h. The behavior of the first peak is already expected from its origin being associated to a GMR, and not an LSP mode, while the behavior of the second peak can be clearly explained from the field pattern in Fig. 7b. It is obvious that because of the field localization and strong confinement in the region between the adjacent disks in the case of the coupled LSP mode associated with the second peak, both r and h should affect its spectral position. Moreover, the behavior of the third and fourth peaks at varying r and h is evident in Figs. 3c and 4c, respectively. It is evident in Fig. 3c that increasing r significantly redshifts both the third and fourth peaks, while the increase of h exerts a very minor effect on the third peak and almost no effect on the fourth peak (Fig. 4c). These features can also be explained by using Fig. 7c–d. One can see that the magnetic field for the conventional and mimicked gap plasmon LSP modes for the both peaks are below the nanodisks, i.e., inside the dielectric (Al_2O_3) region, and therefore, they are associated with the radius of disks, and not with their height.

The input impedance of the entire structure, which is normalized to the free space impedance, can be calculated by using the following formula:

$$Z_{in} = \left(\frac{(1 + S_{11}^2) - S_{21}^2}{(1 - S_{11}^2) - S_{21}^2} \right)^{0.5} \quad (2)$$

where S_{11} and S_{21} are the complex-valued elements of the **S**-matrix, corresponding to the reflection and transmission, respectively. The results are presented in Fig. 9d. In order to have perfect matching with free space, the real part of the normalized input impedance of the structure must be 1, and its imaginary part must be zero [13]. Even an imperfect impedance matching may lead to minimizing the reflection, and thereby, maximizing the absorption. For instance, $Z_{in} = 1.016 - j\,0.029$ at the spectral position of the second absorption peak for the optimized structure, located at 778 nm, which is the cause of the strong absorption. The cause is the same for the third and fourth peaks.

Now, let us revisit some features observed in Fig. 2 once more, by taking into account the results presented in Fig. 10. It is observable that changing the metal of the ultra-thin layer has a

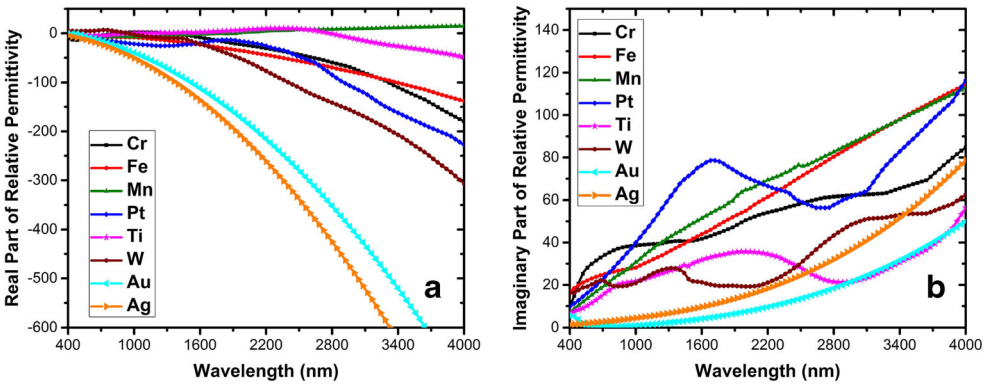

Fig. 10 **a**) Real and **b** imaginary parts of the relative permittivity for Cr, Fe, Mn, Pt, Ti, W, Au, and Ag

much stronger effect on the absorption of the structure compared to changing the metal of the top nanodisk and bottom metal layer. The substantial difference between the performances with different metals in the ultra-thin middle metal layer is attributed to the fact that, as it was observed in the field patterns in Fig. 7, the field is enhanced around this thin layer for IR wavelengths, and the field penetration and absorption inside this layer gets significantly affected by the optical properties of the used metal. It is noticeable from Fig. 2d that Mn provides the best result when being used as the ultra-thin layer. The second best performance has the ultra-thin layer made of Ti. These two materials provide a significantly superior performance as compared to the other metals in the MIR region. As seen in Fig. 10a, Mn and Ti have much smaller modulus of the real part of permittivity compared to the other metals, in the MIR region. Having a small modulus of the real part of permittivity leads to a high field penetration inside Mn and Ti, and their intrinsic metallic loss may lead to stronger absorption. Mn has a smaller modulus of the real part of permittivity and a larger imaginary part of permittivity (higher loss), compared to Ti. This is why using Mn as the ultra-thin layer results in a wider absorption band compared to Ti. Moreover, it can be observed in Fig. 2d that using Au and Ag in the ultra-thin layer leads to a significant narrowing of the absorption band. This issue arises from the similar reason as the one explained above. It can be observed in Fig. 10 that Au and Ag have a much larger modulus of the real part of permittivity and a smaller imaginary part of permittivity compared to the rest of metals. This is a reason why the field penetration, field enhancement, and absorption for Au and Ag cannot be as efficient as for the other metals.

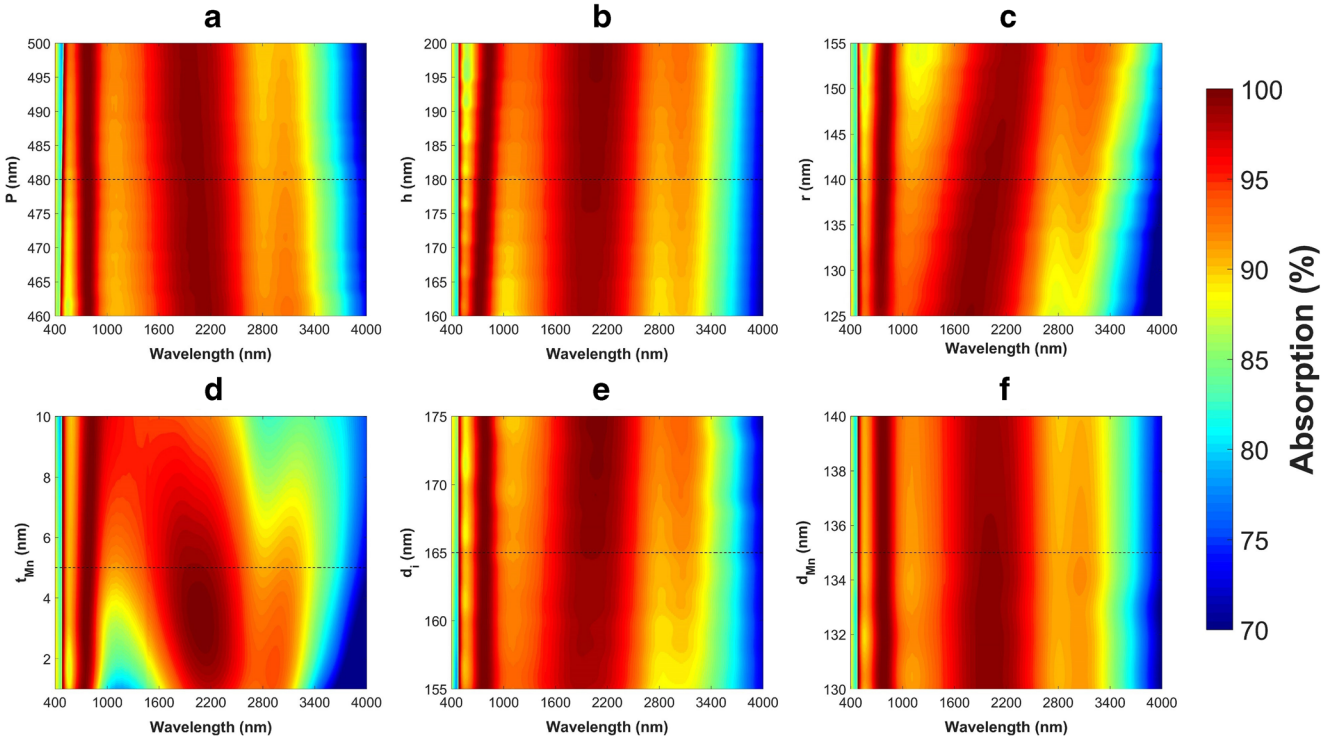

Fig. 11 Color plots of the absorption versus **a** p, **b** h, **c** r, **d** t_{Mn}, **e** d_i, and **f** d_{Mn} and wavelength, for the purpose of demonstration of fabrication tolerance of the optimal structure. The dashed horizontal lines indicate the optimal value of the parameter under study

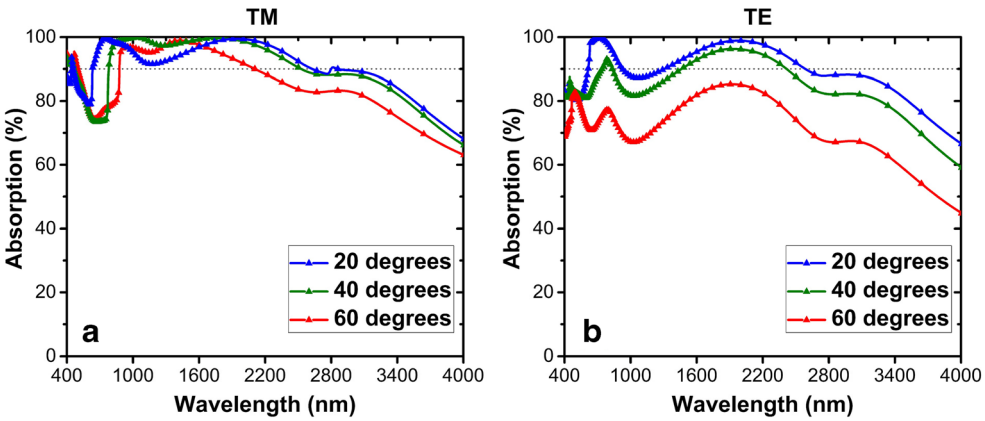

Fig. 12 Absorption spectrum of the optimal structure for oblique incidence angles of 20, 40, and 60 degrees; **a** TM and **b** TE polarizations

Fabrication Tolerance

Next, let us investigate the fabrication tolerance of the structure, which is an important factor for the evaluation of the prospects of mass production. As mentioned earlier, large-scale fabrication and production of the proposed structure is realizable by nanoimprint lithography, since it has only one step of lithography in its fabrication procedure. This technique can resolve sub-100 nm features with a high precision [39].

Fig. 11a–f show the color plots of the absorption versus wavelength for the continuously varying values of p, h, r, t_{Mn}, d_i, and d_{Mn}, respectively, while keeping all the other parameters constant and equal to the ones of the optimized structure. These figures demonstrate the tolerance of the structure's response to the deviations from the design dimensions, which can be a result of fabrication imperfections. The optimal values of the geometrical sizes are shown by the horizontal dashed lines. The response of the structure seems to be most sensitive to the deviations of the thickness of the Mn layer (t_{Mn}), as shown in Fig. 11d. In particular, one can see that the deviations of t_{Mn} from the selected value can lead to a band narrowing (at larger t_{Mn}) and a band splitting (at smaller t_{Mn}). In addition, as can be seen in Fig. 11c, deviations from the optimal value of r may lead to an insignificant redshift or blueshift in the position of the second, third, and fourth peaks, but the general behavior of the absorption band does not get affected significantly. The response has a very good robustness to the introduced variations in p, h, d_i, and d_{Mn}, although some relatively minor changes in the bandwidth are possible. All the plots in Fig. 11 confirm that the suggested design has a very good fabrication tolerance to possible deviations from the optimal values. This confirms that, in addition to comprising cost-effective materials, this structure is fabrication tolerant, and therefore, it is a very good candidate for future mass production.

Polarization and Incidence Angle Sensitivity

As the final step, we investigate the absorption behavior of the structure for different angles of incidence for both polarizations. Figure 12a, b show absorption versus wavelength for incidence angles of 20, 40, and 60 degrees for TM and TE polarizations, respectively. In general, the absorption band is narrowing when the angle is increased. However, at certain wavelengths, for the case of the incidence angle of 40 degrees and TM polarization in Fig. 12a, absorption is almost perfect, e.g., $A > 97\%$, within the range of $818 < \lambda < 2147$ nm. The results show that the absorption remains high in a wide wavelength range for TM polarization up to incidence angles as large as 60 degrees; TE polarization is more sensitive to the incidence angle variations. In spite of this, a rather wide band of $A > 90\%$ can exist at least up to 40 degrees.

Conclusion

An ultra-broadband, nearly perfect absorber is designed, analyzed, and characterized in detail. The studied structure is actually a top-layer-patterned MIM structure with Ti-Al_2O_3-Ti configuration, with an ultra-thin 5 nm layer of Mn embedded into the dielectric (Al_2O_3) layer. It has been shown that adding just a very thin layer of Mn widens the band from 274 nm to 2800 nm, i.e., it leads to a tenfold increase in the bandwidth. This allows covering the visible, NIR, and partially MIR range, while it does not need additional lithography steps and does not add much to the overall fabrication complexity of the structure. The proposed structure has the relative absorption bandwidth of 149%, which is probably the best result obtained so far for such structures. It has been shown that it keeps high absorption for both TM and TE polarizations up to large angles. Since the structure only needs one step of lithography in its fabrication procedure, with the dimensions of lithographic patterns being over 180 nm, and with the high fabrication tolerance, its mass production can be easily realized by using nanoimprint lithography technology. Taking this fact into consideration along with the unprecedentedly ultra-broadband, nearly perfect absorption, one can conclude that the proposed absorber is very promising for photovoltaic and thermal emission applications. The use of Mn for one of the absorber components, the suggested design procedure, and obtained numerical results can serve, along with the

performed physical analysis, as a good starting point for design of a wide class of ultra-wideband absorbers that meet the requirements of a broad spectrum of applications, ranging from photovoltaics and solar cells to shielding and optical communication filtering.

Acknowledgments Ekmel Ozbay acknowledges partial support from the TUBA. Amin Khavasi also acknowledges Research Office of Sharif University of Technology.

Funding Information Narodowe Centrum Nauki (NCN), Poland (DEC-2015/17/B/ST3/00118–Metasel); Turkish Academy of Sciences (TUBA); Research Office of Sharif University of Technology.

References

1. Wang ZY, Tong Z, Ye QX, Hu H, Nie X, Yan C, Shang W, Song CY, Wu JB, Wang J, Bao H, Tao P, Deng T (2017) Dynamic tuning of optical absorbers for accelerated solar-thermal energy storage. Nat Commun 8:1478
2. McMeekin DP, Sadoughi G, Rehman W, Eperon GE, Saliba M, Horantner MT, Haghighirad A, Sakai N, Korte L, Rech B, Johnston MB, Herz LM, Snaith HJ (2016) A mixed-cation lead mixed-halide perovskite absorber for tandem solar cells. Science 351(6269):151–155
3. Liu N, Mesch M, Weiss T, Hentschel M, Giessen H (2010) Infrared perfect absorber and its application as plasmonic sensor. Nano Lett 10(7):2342–2348
4. Tittl A, Mai P, Taubert R, Dregely D, Liu N, Giessen H (2011) Palladium-based plasmonic perfect absorber in the visible wavelength range and its application to hydrogen sensing. Nano Lett 11(10):4366–4369
5. Li W, Valentine J (2014) Metamaterial perfect absorber based hot electron photodetection. Nano Lett 14(6):3510–3514
6. Bessonov AA, Allen M, Liu YL, Malik S, Bottomley J, Rushton A, Medina-Salazar I, Voutilainen M, Kallioinen S, Colli A, Bower C, Andrew P, Ryhanen T (2017) Compound quantum dot-perovskite optical absorbers on graphene enhancing short-wave infrared photodetection. ACS Nano 11(6):5547–5557
7. Fan KB, Suen JY, Liu XY, Padilla WJ (2017) All-dielectric metasurface absorbers for uncooled terahertz imaging. Optica 4(6):601–604
8. Cahill DG, Braun PV, Chen G, Clarke DR, Fan SH, Goodson KE, Keblinski P, King WP, Mahan GD, Majumdar A, Maris HJ, Phillpot SR, Pop E, Shi L (2014) Nanoscale thermal transport. II. 2003-2012. Appl Phys Rev 1(1):011305
9. Cao TC, Xu KL, Chen GM, Guo CY (2013) Poly (ethylene terephthalate) nanocomposites with a strong UV-shielding function using UV-absorber intercalated layered double hydroxides. RSC Adv 3(18):6282–6285
10. Khalid T, Albasha L, Qaddoumi N, Yehia S (2017) Feasibility study of using electrically conductive concrete for electromagnetic shielding applications as a substitute for carbon-laced polyurethane absorbers in anechoic chambers. IEEE Trans Antenn Propag 65(5): 2428–2435
11. Nguyen TT, Lim S (2018) Design of metamaterial absorber using eight-resistive-arm cell for simultaneous broadband and wide-incidence-angle absorption. Sci Rep 8:6633
12. Serebryannikov AE, Nojima S, Ozbay E (2014) One-way absorption of terahertz waves in rod-type and multilayer structures containing polar dielectrics. Phys Rev B 90:235126
13. Rodriguez-Ulibarri P, Beruete M, Serebryannikov AE (2017) One-way quasiplanar terahertz absorbers using nonstructured polar dielectric layers. Phys Rev B 96:155148
14. Lin YY, Cui YX, Ding F, Fung KH, Ji T, Li DD, Hao YY (2017) Tungsten based anisotropic metamaterial as an ultra-broadband absorber. Opt Mater Express 7(2):606–617
15. Guo WL, Liu YX, Han TC (2016) Ultra-broadband infrared metasurface absorber. Opt Express 24(18):20586–20592
16. Ding F, Dai J, Chen YT, Zhu JF, Jin Y, Bozhevolnyi SI (2016) Broadband near-infrared metamaterial absorbers utilizing highly lossy metals. Sci Rep 6:39445
17. Ghobadi A, Hajian H, Gokbayrak M, Dereshgi SA, Toprak A, Butun B, Ozbay E (2017) Visible light nearly perfect absorber: an optimum unit cell arrangement for near absolute polarization insensitivity. Opt Express 25(22):27624–27634
18. Hubarevich A, Kukhta A, Demir HV, Sun X, Wang H (2015) Ultrathin broadband nanostructured insulator-metal-insulator-metal plasmonic light absorber. Opt Express 23(8):9753–9761
19. Chen K, Adato R, Altug H (2012) Dual-band perfect absorber for multispectral plasmon-enhanced infrared spectroscopy. ACS Nano 6(9):7998–8006
20. Zhang CL, Huang C, Pu MB, Song JK, Zhao ZY, Wu XY, Luo XG (2017) Dual-band wide-angle metamaterial perfect absorber based on the combination of localized surface plasmon resonance and Helmholtz resonance. Sci Rep 7:5652
21. Cong JW, Zhou ZQ, Yun BF, Lv L, Yao HB, Fu YH, Ren NF (2016) Broadband visible-light absorber via hybridization of propagating surface plasmon. Opt Lett 41(9):1965–1968
22. Li Q, Gao JS, Yang HG, Liu H, Wang XY, Li ZZ, Guo X (2017) Tunable plasmonic absorber based on propagating and localized surface plasmons using metal-dielectric-metal structure. Plasmonics 12(4):1037–1043
23. Li ZY, Butun S, Aydin K (2015) Large-area, lithography-free super absorbers and color filters at visible frequencies using ultrathin metallic films. ACS Photonics 2(2):183–188
24. Aalizadeh M, Serebryannikov AE, Khavasi A, Vandenbosch GAE, Ozbay E (2018) Toward electrically tunable, lithography-free, ultrathin color filters covering the whole visible Spectrum. Sci Rep 8: 11316
25. Luo SW, Zhao J, Zuo DL, Wang XB (2016) Perfect narrow band absorber for sensing applications. Opt Express 24(9):9288–9294
26. Tsakmakidis KL, Boardman AD, and Hess O (2007) "Trapped rainbow" storage of light in metamaterials, Nature 450(7168): 397–401
27. Aydin K, Ferry VE, Briggs RM, Atwater HA (2011) Broadband polarization-independent resonant light absorption using ultrathin plasmonic super absorbers. Nat Commun 2:517
28. Ghobadi A, Hajian H, Dereshgi SA, Bozok B, Butun B, Ozbay E (2017) Disordered nanohole patterns in metal-insulator multilayer for ultra-broadband light absorption: atomic layer deposition for lithography free highly repeatable large scale multilayer growth. Sci Rep 7:15079
29. Dereshgi SA, Okyay AK (2016) Large area compatible broadband superabsorber surfaces in the VIS-NIR spectrum utilizing metal-insulator-metal stack and plasmonic nanoparticles. Opt Express 24(16):17644–17653
30. Ghobadi A, Dereshgi SA, Hajian H, Birant G, Butun B, Bek A, Ozbay E (2017) 97 percent light absorption in an ultrabroadband frequency range utilizing an ultrathin metal layer: randomly oriented, densely packed dielectric nanowires as an excellent light trapping scaffold. Nanoscale 9(43):16652–16660

31. Li ZY, Palacios E, Butun S, Kocer H, Aydin K (2015) Omnidirectional, broadband light absorption using large-area, ultrathin lossy metallic film coatings. Sci Rep 5:15137
32. Aalizadeh M, Khavasi A, Butun B, Ozbay E (2018) Large-area, cost-effective, ultra-broadband perfect absorber utilizing manganese in metal-insulator-metal structure. Sci Rep 8:9162
33. Ding F, Mo L, Zhu JF, He SL (2015) Lithography-free, broadband, omnidirectional, and polarization-insensitive thin optical absorber. Appl Phys Lett 106:061108
34. Lumerical Solutions Inc., http://www.lumerical.com/tcad-products/fdtd/
35. CST Inc., https://www.cst.com/products/cstmws/solvers/transientsolver/
36. Lebib A, Chen Y, Bourneix J, Carcenac F, Cambril E, Couraud L, Launois H (1999) Nanoimprint lithography for a large area pattern replication. Microelectron Eng 46(1–4):319–322
37. Palik ED, Handbook of optical constants of solids (Academic Press, 1998)
38. Querry MR, *Optical constants of minerals and other materials from the millimeter to the ultraviolet* (US Army Armament, Munitions & Chemical Research, Development & Engineering Center, 1987)
39. Wood DL, Nassau K, Kometani TY, Nash DL (1990) Optical-properties of cubic hafnia stabilized with Yttria. Appl Opt 29(4):604–607
40. Siefke T, Kroker S, Pfeiffer K, Puffky O, Dietrich K, Franta D, Ohlidal I, Szeghalmi A, Kley EB, Tunnermann A (2016) Materials pushing the application limits of wire grid polarizers further into the deep ultraviolet spectral range. Adv Opt Mater 4(11):1780–1786
41. Ozbay E (2006) Plasmonics: merging photonics and electronics at nanoscale dimensions. Science 311(5758):189–193
42. Kuo WK, Hsu CJ (2017) Two-dimensional grating guided-mode resonance tunable filter. Opt Express 25(24):29642–29649
43. Boonruang S, Greenwell A, Moharam MG (2006) Multiline two-dimensional guided-mode resonant filters. Appl Opt 45(22):5740–5747
44. Boonruang S, Greenwell A, Moharam MG (2007) Broadening the angular tolerance in two-dimensional grating resonance structures at oblique incidence. Appl Opt 46(33):7982–7992
45. Della Giovampaola C, Engheta N (2016) Plasmonics without negative dielectrics. Phys Rev B 93:195152